








# Interplay between spin proximity effect and charge-dependent exciton dynamics in MoSe<sub>2</sub>/CrBr<sub>3</sub> van der Waals heterostructures

T. P. Lyons <sup>1✉</sup>, D. Gillard <sup>1</sup>, A. Molina-Sánchez <sup>2</sup>, A. Misra<sup>3,4</sup>, F. Withers <sup>5</sup>, P. S. Keatley<sup>5</sup>, A. Kozikov<sup>3</sup>, T. Taniguchi <sup>6</sup>, K. Watanabe <sup>6</sup>, K. S. Novoselov<sup>3,7,8</sup>, J. Fernández-Rossier<sup>2</sup> & A. I. Tartakovskii <sup>1✉</sup>

Semiconducting ferromagnet-nonmagnet interfaces in van der Waals heterostructures present a unique opportunity to investigate magnetic proximity interactions dependent upon a multitude of phenomena including valley and layer pseudospins, moiré periodicity, or exceptionally strong Coulomb binding. Here, we report a charge-state dependency of the magnetic proximity effects between MoSe<sub>2</sub> and CrBr<sub>3</sub> in photoluminescence, whereby the valley polarization of the MoSe<sub>2</sub> trion state conforms closely to the local CrBr<sub>3</sub> magnetization, while the neutral exciton state remains insensitive to the ferromagnet. We attribute this to spin-dependent interlayer charge transfer occurring on timescales between the exciton and trion radiative lifetimes. Going further, we uncover by both the magneto-optical Kerr effect and photoluminescence a domain-like spatial topography of contrasting valley polarization, which we infer to be labyrinthine or otherwise highly intricate, with features smaller than 400 nm corresponding to our optical resolution. Our findings offer a unique insight into the interplay between short-lived valley excitons and spin-dependent interlayer tunneling, while also highlighting MoSe<sub>2</sub> as a promising candidate to optically interface with exotic spin textures in van der Waals structures.

<sup>1</sup>Department of Physics and Astronomy, The University of Sheffield, Sheffield S3 7RH, UK. <sup>2</sup>QuantaLab, International Iberian Nanotechnology Laboratory, Braga 4715-330, Portugal. <sup>3</sup>School of Physics and Astronomy, The University of Manchester, Manchester M13 9PL, UK. <sup>4</sup>Department of Physics, Indian Institute of Technology Madras (IIT Madras), Chennai, India. <sup>5</sup>Department of Physics and Astronomy, University of Exeter, Exeter EX4 4QL, UK. <sup>6</sup>National Institute for Materials Science, Tsukuba, Ibaraki 305-0044, Japan. <sup>7</sup>Centre for Advanced 2D Materials, National University of Singapore, Singapore 117546, Singapore. <sup>8</sup>Chongqing 2D Materials Institute, Liangjiang New Area, Chongqing 400714, China. ✉email: [t.lyons@sheffield.ac.uk](mailto:t.lyons@sheffield.ac.uk); [a.tartakovskii@sheffield.ac.uk](mailto:a.tartakovskii@sheffield.ac.uk)

Few of the materials which have underpinned solid-state physics research over the past century now lack a 2-dimensional crystalline analog<sup>1,2</sup>. This is keenly exemplified by recent discoveries of long-range magnetic order persisting into the monolayer limit in 2-dimensional van der Waals materials<sup>3–7</sup>. However, the true potential of layered crystals lies not simply in having access to a selection of atomically thin proxies for conventional materials, but rather the ability to easily stack and combine these different materials into arbitrarily designed van der Waals heterostructures<sup>8</sup>. Not only are such composites free of dangling bonds and growth-related lattice matching constraints, but also exhibit cumulative and hybridized properties superior to those of the constituent layers, and as such represent the building blocks for future generations of nanoscale information technologies<sup>9–14</sup>.

In this context, the discovery of 2-dimensional magnets in particular realizes a step-change for the nascent field of wholly van der Waals based spintronics<sup>5,15–22</sup>. One such material currently experiencing a resurgence of interest is chromium tribromide ( $\text{CrBr}_3$ )<sup>7,23–26</sup>, a layered ferromagnetic semiconductor with Curie temperature 37 K and magnetization  $3.85\mu_B$  per Cr atom along the easy  $c$ -axis<sup>27</sup>. Recent work suggests that, in stark contrast to few-layer  $\text{CrI}_3$  and  $\text{CrCl}_3$  flakes which both exhibit antiferromagnetic interlayer ordering<sup>4,22,28</sup>, the interlayer exchange in exfoliated  $\text{CrBr}_3$  is ferromagnetic, although can depend on stacking order<sup>7,23,24,26</sup>.

The incorporation of this emerging family of magnetic materials with optically active transition metal dichalcogenides (TMDs) is expected to combine the advantageous chiral optical selection rules and spin-valley locking of TMDs with the highly correlated and field-responsive long-range ordering inherent to magnets<sup>17,29–31</sup>. Proximity effects between monolayer TMDs and van der Waals ferromagnets have so far manifested as enhanced valley Zeeman splitting and/or modifications to the photoluminescence (PL) intensity<sup>22,24,30,32</sup>. Where changes in the

circular polarization degree of PL are reported, significantly broadened linewidths preclude the extraction of useful spectral information, and individual excitonic states cannot be resolved<sup>30</sup>.

In this work, we study a van der Waals interface formed between the TMD molybdenum diselenide ( $\text{MoSe}_2$ ) and ferromagnetic  $\text{CrBr}_3$ . While the interlayer band alignment is nominally type-II, with the global conduction band minimum found in  $\text{CrBr}_3$ , a strong spin polarization of the  $\text{CrBr}_3$  conduction bands gives rise to spin-dependent interlayer charge transfer rates for electrons tunneling from  $\text{MoSe}_2$  to  $\text{CrBr}_3$ . This spin-dependent non-radiative decay channel causes a valley-dependent quenching of  $\text{MoSe}_2$  photoluminescence intensity, leading to a strongly enhanced degree of circular polarization (DOCP). Crucially, the DOCP is observed only in the  $\text{MoSe}_2$  trion state, rather than the neutral exciton, thereby providing insight into the interlayer tunneling timescales, which we infer to lie between the exciton and trion radiative lifetimes. By performing wide-field polar Kerr microscopy, we both confirm that the  $\text{MoSe}_2$  trion DOCP is an accurate indicator of local  $\text{CrBr}_3$  magnetization, and gain information about the characteristic magnetic domain length-scales in our sample. Our findings shed new light on the mechanisms of interlayer charge transfer in TMD/magnet van der Waals interfaces. Moreover, our work highlights the importance of optical resolution when studying this new class of layered magnetic materials.

## Results

**$\text{MoSe}_2/\text{CrBr}_3$  van der Waals heterostructures.** The sample consists of a monolayer of  $\text{MoSe}_2$  placed directly on top of  $\sim 7$ – $8$  nm thick multilayered  $\text{CrBr}_3$ , with few-layer hBN encapsulating the structure on both sides, as shown in Fig. 1a. The hBN encapsulation is necessary here owing to the extreme environmental sensitivity of exfoliated  $\text{CrBr}_3$ , a property shared also with  $\text{CrI}_3$ , in which degradation occurs rapidly under exposure to air and moisture, in a reaction catalyzed by light<sup>34</sup>. The residue-free transfer techniques

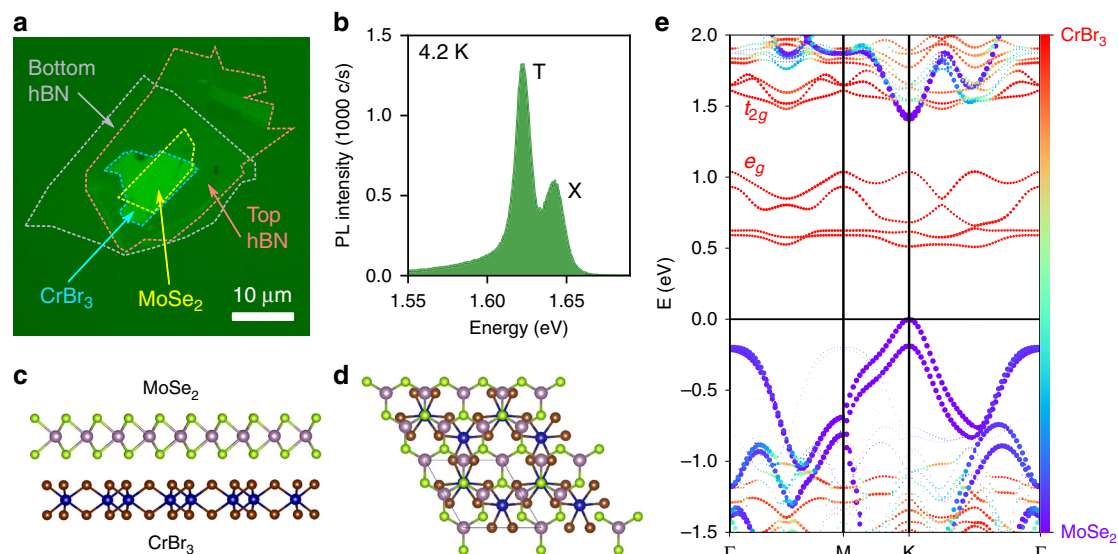


**Fig. 1**  $\text{MoSe}_2/\text{CrBr}_3$  van der Waals heterostructures. **a** Microscope image of the sample in this work showing multi-layered  $\text{CrBr}_3$ , monolayer  $\text{MoSe}_2$ , and hBN encapsulation layers. **b** Photoluminescence spectrum from the sample under continuous-wave laser excitation at 1.946 eV and a sample temperature of 4.2 K. Neutral exciton (X) and trion (T) peaks are visible. **c**, **d** Schematics of a  $\text{MoSe}_2/\text{CrBr}_3$  heterobilayer structure used in the density functional theory calculations, viewed from the side (**c**) and top (**d**), where the supercell is highlighted. Here, the experimental lattice constant of monolayer  $\text{MoSe}_2$  is applied to both layers, in order to simplify the calculations, along with setting the relative crystallographic twist angle to zero between the layers (see Supplementary Note 1). Crystal images were produced using VESTA software<sup>33</sup>. **e** The DFT calculated electronic band structure of the  $\text{MoSe}_2/\text{CrBr}_3$  heterobilayer, projected on the host material. The global valence band maximum is localized in  $\text{MoSe}_2$  at  $E = 0$ . The green band color indicates hybridization between the two materials. The  $e_g$ -orbitals have spin polarization opposite to the  $t_{2g}$ -orbitals.

used during fabrication (see Methods) ensure full contact between the MoSe<sub>2</sub> and CrBr<sub>3</sub>, such that trapped contaminants do not inhibit the interlayer charge transfer and proximity induced magnetic exchange effects. Photoluminescence (PL) from the sample at 4.2 K under non-resonant optical excitation at 1.946 eV displays a spectrum quite characteristic of MoSe<sub>2</sub>, with a high energy peak ascribed to the neutral exciton (X) and a lower energy peak attributed to the charged exciton, or trion (T) (Fig. 1b)<sup>35,36</sup>. However, the emission intensity from the sample is far lower than typical for exfoliated MoSe<sub>2</sub>, indicating a quenching of PL due to loss of photocarriers from MoSe<sub>2</sub> into CrBr<sub>3</sub>, reducing the quantum yield.

Density functional theory (DFT) calculations of the electronic band structure of a MoSe<sub>2</sub>/CrBr<sub>3</sub> heterobilayer (Figs. 1c, d) indicate a type-II interlayer band alignment, with the global conduction band (CB) minimum located in the CrBr<sub>3</sub> layer, as shown in Fig. 1e. As the material bandgaps depend sensitively on ligand electronegativity, the exact interlayer band alignment at the interface depends heavily on the elemental compositions of each layer<sup>37</sup> (For details of the DFT calculations see Supplementary Note 1). Photogenerated electrons are predicted to scatter from the MoSe<sub>2</sub> CB into the CrBr<sub>3</sub> CB, introducing an additional non-radiative decay channel, corroborating with the observed suppressed luminescence intensity. Such interlayer charge transfer may be aided by electronic interlayer hybridization between the two materials, seen in Fig. 1e as green-shaded regions. Any instances of hybridization would be expected to lead to efficient interlayer charge transfer, via elastic scattering events. Additionally, this heterostructure band alignment suggests that a static electron doping cannot exist in the MoSe<sub>2</sub> layer, while holes will accumulate in the MoSe<sub>2</sub> valence band (VB) as electrons tunnel out of the CB non-radiatively. Therefore, we attribute the observed trion luminescence to positively charged excitons, whereby neutral excitons bind to resident holes in the MoSe<sub>2</sub> VB<sup>30,35</sup>.

A crucial feature of our experiment is that our laser, at 1.946 eV, lies directly in an absorption minimum of CrBr<sub>3</sub><sup>38–40</sup>. In this way, we ensure that photoexcitation occurs only in MoSe<sub>2</sub>, and so no electron-hole pairs are created in CrBr<sub>3</sub>. Therefore, with the exception of possible electrostatic discharge when the interface is first formed during sample fabrication, we can confidently neglect appreciable hole tunneling from CrBr<sub>3</sub> to MoSe<sub>2</sub>. As confirmation that our laser is not being absorbed, we search for direct CrBr<sub>3</sub> luminescence, reported at 1.35 eV under 1.77 eV illumination<sup>25</sup>. Despite rigorous searching, we observe nothing but MoSe<sub>2</sub> PL between the laser energy and the limit of our detector sensitivity, ~1.1 eV, consistent with CrBr<sub>3</sub> being transparent to our laser.

The calculated electronic band structure in Fig. 1e also reveals a strong exchange splitting of the CrBr<sub>3</sub> CB, which is comprised of Cr<sup>3+</sup>*d*-orbitals. Bands arising from the majority-spin *e<sub>g</sub>* orbitals can be seen in red between 0.5 and 1 eV, while the minority-spin *t<sub>2g</sub>* orbitals form bands at 1.5 eV and above<sup>41,42</sup>. Importantly, below the CrBr<sub>3</sub> Curie temperature ~ 37 K, these two sets of bands are oppositely spin-polarized out of the sample plane. This is intrinsically tied to the local CrBr<sub>3</sub> magnetization, such that when the magnetization is flipped between pointing up or down out of the plane, the spin polarization of these two sets of bands reverses. Since the *e<sub>g</sub>* orbitals constitute the majority-spin, they are spin-↑ (spin-↓) when the local CrBr<sub>3</sub> magnetization points upwards (downwards) out of the sample plane, while the *t<sub>2g</sub>* orbitals are spin-↓ (spin-↑).

Although our sample is not a heterobilayer, but rather multi-layered CrBr<sub>3</sub>, we expect any magnetic proximity effects to arise primarily from the topmost CrBr<sub>3</sub> layer, owing to the very short range of exchange interactions and interlayer orbital wavefunction overlap<sup>22,43</sup>. We confirm this by calculating and comparing the band structures of MoSe<sub>2</sub>/1L CrBr<sub>3</sub> and MoSe<sub>2</sub>/2L CrBr<sub>3</sub>, and

observe only negligible differences between the two (see Supplementary Note 2).

**Polarization resolved magneto-photoluminescence.** In order to gain insight into the valley pseudospin dynamics in our sample, we detect PL in  $\sigma^+$  and  $\sigma^-$  circular polarizations while sweeping an external magnetic field (*B*) perpendicular to the sample plane, within the range  $B = \pm 200$  mT, in both forward (negative to positive) and backward (positive to negative) sweep directions, at 4.2 K. A *B*-field orientation upwards (downwards) out of the plane is positive (negative). Fig. 2a shows the  $\sigma^+$  polarized PL as a function of emitted photon energy and *B*-field, in the forward sweep direction. As can be seen, the trion intensity sharply increases at  $B = -20$  mT, followed by a steady further increase, until the intensity reaches a plateau at  $B \sim 50$  mT. This striking response must be attributed to the influence of CrBr<sub>3</sub>, as the PL intensity of an isolated MoSe<sub>2</sub> monolayer would change only negligibly under the application of such weak external *B*-fields as used here<sup>44,45</sup>. In stark contrast, the exciton emission, notably distinct from the trion, exhibits no observable change in intensity.

Bright neutral excitons are comprised of an electron-hole pair located in either the K or K' valley, corresponding to the  $\sigma^+$  or  $\sigma^-$  polarization state of the emitted photon (Fig. 2b)<sup>29</sup>. To form a positively charged trion, the exciton binds to an additional hole in the opposite valley (Fig. 2b)<sup>35,46</sup>. This intervalley ground state is highly favored over the intravalley trion configuration, for which the large ~200 meV spin-orbit coupling strength in the VB is prohibitive<sup>35,46–48</sup>. The electron spin is tied to the emission helicity owing to optical selection rules and spin-valley locking<sup>29,46</sup>.

To elucidate the trion magneto-optical response, we plot the integrated trion intensity in both circular polarizations, in both forwards and backwards *B*-field sweep directions, as shown in Fig. 2c. As can be seen, the trion intensities in opposite polarizations behave exactly symmetrically, such that when the intensity of one polarization decreases the other increases by the same amount. In both sweep directions, the intensities invert as *B* passes through zero, indicating a clear reversal of trion valley populations when very small *B*-fields are applied. A specific response to the sweep direction which is symmetric about zero-field, as seen here, is a hallmark of ferromagnetism, confirming the influence of CrBr<sub>3</sub> on the MoSe<sub>2</sub> trion state valley polarization.

A powerful tool to investigate the valley pseudospin dynamics in the sample is the DOCP,  $(I_{\sigma^+} - I_{\sigma^-}) / (I_{\sigma^+} + I_{\sigma^-})$ , of the emitted luminescence. Fig. 2d presents the DOCP as a function of photon energy and applied *B*-field, in the forward sweep direction. Here, a very prominent trion switching can be seen between robust positive and negative DOCP, while the exciton state remains apparently insensitive to any interactions with CrBr<sub>3</sub>. Plotting the DOCP using integrated intensities, in both sweep directions, as shown in Fig. 2e, brings the sweep direction-dependent response into sharp focus. While the exciton remains at zero, the trion state follows a sweep-dependent path when switching between the two valley polarized extremes, revealing the existence of two hysteretic lobes in the DOCP. We have fabricated and studied an additional 2 samples, both of which reproduce the trion DOCP sensitivity and exciton insensitivity observed in sample 1 (See Supplementary Note 3). Furthermore, by heating the sample under a fixed applied *B*-field, we observe the DOCP to tend to zero above the reported Curie temperature of CrBr<sub>3</sub>, ~ 37 K (See Supplementary Note 4)<sup>27</sup>.

**Spin-dependent interlayer charge transfer.** Ostensibly, an enhanced DOCP in MoSe<sub>2</sub> trion luminescence indicates a finite

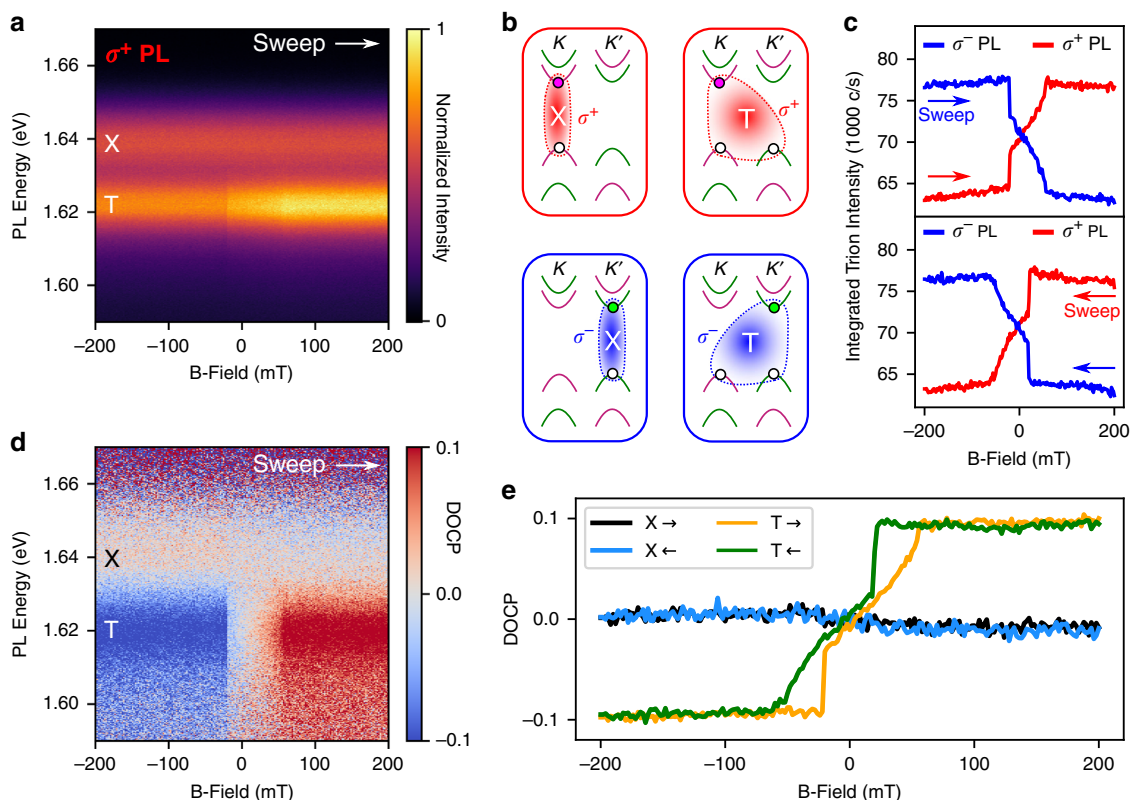


**Fig. 2 Magneto-photoluminescence of MoSe<sub>2</sub>/CrBr<sub>3</sub> heterostructures.** **a** Photoluminescence (PL) intensity in  $\sigma^+$  circular polarization as a function of photon energy and external  $B$ -field, in the forward sweep direction. The neutral exciton (X) and trion (T) are labeled. **b** Schematics of the electron-hole valley configurations of the two ground-state optically bright neutral excitons and positive trions in monolayer MoSe<sub>2</sub>, which emit either a  $\sigma^+$  or  $\sigma^-$  polarized photon upon recombination. The pink (green) electron is spin  $\uparrow$  ( $\downarrow$ ), and the hole is white, regardless of spin. Spin-valley locking ties the electron spin to the emission polarization. **c** Integrated trion PL intensity in both circular polarizations, for the forward (upper panel) and backward (lower panel)  $B$ -field sweep directions. **d** Degree of circular polarization (DOCP) as a function of photon energy and  $B$ -field, in the forward sweep direction. **e** DOCP of the exciton and trion states calculated from integrated intensities, shown for both sweep directions, revealing hysteresis type behavior in the trion. The error in DOCP for this figure is  $\sim \pm 0.005$ .

valley polarization in the resident carrier population. However, in this case, a hole valley polarization may be ruled out as the origin of the observed trion DOCP for three reasons. Firstly, any imbalance between the itinerant carrier populations of the two valleys leads not only to a change in trion intensity, but also to an opposite and proportional change in exciton intensity, owing to the intervalley nature of the trion ground state<sup>44</sup>. We observe no corresponding change in exciton intensity in Fig. 2a, and no mirroring of the trion DOCP by the exciton DOCP in Figs. 2d and e. Secondly, the observed trion DOCP cannot be due to a suppression of intervalley relaxation, as the sign of the DOCP is independent of the polarization state of the laser, and so the system retains no memory of optical valley initialization (see Supplementary Note 5). Thirdly, our DFT calculations predict a negligible proximity induced spin splitting in the MoSe<sub>2</sub> VB maxima, thereby precluding the generation of a static valley polarization in the itinerant hole population in thermal equilibrium. The band dependence of the proximity induced spin splitting is ultimately related to their different orbital content, with the VB orbitals being oriented preferably in the molybdenum plane, and so experiencing a weak proximity effect. The orbitals constituting the MoSe<sub>2</sub> CB edges do protrude more out of the molybdenum plane, and so do experience a modest spin splitting due to proximity, which we measure to be  $< 0.5$  meV (Supplementary Notes 1 and 6). Regardless, this splitting is in the CB and so cannot generate a static hole valley polarization in the VB.

Therefore, rather than a static hole valley polarization, we attribute the observed DOCP to spin-dependent interlayer electron transfer, which translates to valley-dependent charge leakage from MoSe<sub>2</sub> owing to the spin-valley locking effect. Similar results have previously been observed in conventional ferromagnet-quantum well systems<sup>49</sup>. The particular interlayer band alignment in this structure results in the MoSe<sub>2</sub> CB being resonant only with the minority-spin ( $t_{2g}$ ) bands of CrBr<sub>3</sub>, while the majority-spin ( $e_g$ ) bands are non-resonant by several hundred meV (Fig. 1e). Therefore, we expect that photogenerated electrons in the MoSe<sub>2</sub> CB will be able to tunnel into the CrBr<sub>3</sub> CB more efficiently if they are spin aligned with the CrBr<sub>3</sub> minority-spin states. In order to tunnel into the majority-spin bands, multiple phonon scattering or high energy Auger-like interactions would be required, resulting in poor tunneling efficiency (Fig. 3a). We also note the aforementioned lack of absorption of our laser by CrBr<sub>3</sub>, which ensures that dynamic hole transfer (spin-dependent or otherwise) from CrBr<sub>3</sub> into MoSe<sub>2</sub> can safely be neglected. Consequently, we can be confident that the observed trion DOCP arises purely from electron tunneling from MoSe<sub>2</sub> into CrBr<sub>3</sub>, which introduces an additional non-radiative decay for K or K' valley trion states, depending on the CrBr<sub>3</sub> magnetization.

We note that our PL signal is comparably quenched in both  $\sigma^+$  and  $\sigma^-$  polarizations, yet shows a 10% DOCP in the trion state. We attribute this to a complex interplay between exciton valley dynamics and spin-dependent interlayer charge transfer in our sample. In MoSe<sub>2</sub>, the exciton dispersion experiences an energy



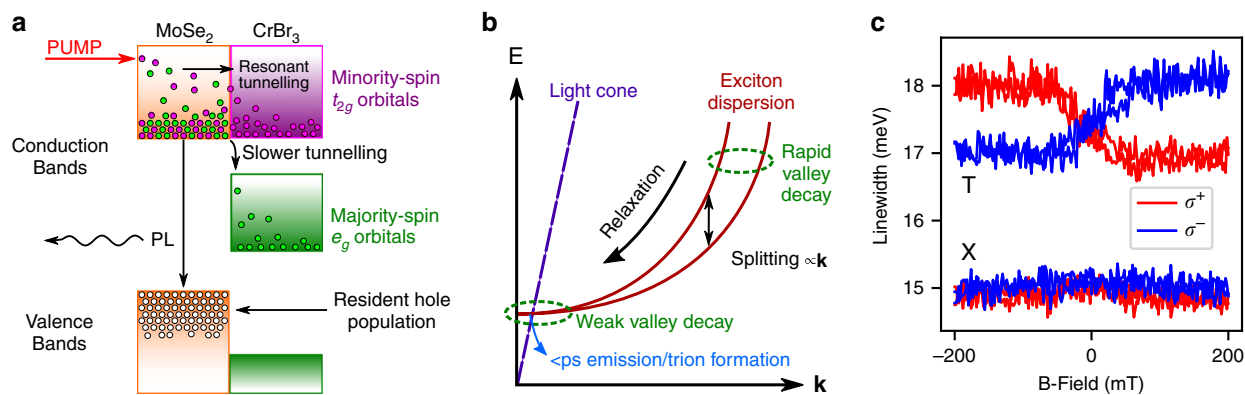


**Fig. 3 Spin-dependent interlayer tunneling.** **a** Schematic of spin-dependent interlayer charge transfer over the MoSe<sub>2</sub>/CrBr<sub>3</sub> interface. The type-II band alignment precludes a static electron doping in MoSe<sub>2</sub>, and so we infer a resident hole population. In CrBr<sub>3</sub>, the CB is strongly split into oppositely spin-polarized bands. Only the minority-spin bands are resonant with the MoSe<sub>2</sub> CB. Upon optical injection of electron-hole pairs, the electrons may tunnel from MoSe<sub>2</sub> to CrBr<sub>3</sub>, with efficiency depending on their spin (green or purple indicate opposite spin). As CrBr<sub>3</sub> is transparent at our laser energy, absorption is negligible, and so we expect no appreciable dynamic hole transfer from CrBr<sub>3</sub> to MoSe<sub>2</sub>. **b** Diagram of exciton dispersion in MoSe<sub>2</sub>, with an energy splitting (the L-T splitting, see main text) proportional to in-plane wavevector **k**. The L-T splitting acts as an effective magnetic field inducing valley pseudospin relaxation in the presence of disorder scattering. Outside the light cone, efficient valley depolarization prevents spin-dependent tunneling from influencing the eventual DOCP. At low **k**, the spin-dependent tunneling is able to influence the DOCP observed in PL. At vanishing center of mass momentum, the exciton population either radiatively recombines (sub-ps) or else binds to a resident hole to form a long-lived trion valley state, which will be susceptible to spin-dependent tunneling. **c** Polarization resolved PL linewidths of the exciton (X) and trion (T). The trion linewidth shows opposing behavior in different polarizations, indicating that the lifetime is influenced by spin-dependent interlayer tunneling. The exciton has a constant linewidth, indicating insensitivity to CrBr<sub>3</sub> magnetization.

splitting between excitons with dipole moment parallel (longitudinal, L) or perpendicular (transverse, T) to their in-plane wavevector, **k**, arising from the long range electron-hole exchange interaction<sup>50,51</sup>. This L-T splitting is linearly proportional to **k** outside the light cone, and manifests as an effective magnetic field acting on the exciton valley pseudospin, causing precession and associated valley depolarization, aided by disorder scattering<sup>50–52</sup>. Consequently, valley depolarization is extremely efficient (<0.1 ps<sup>53</sup>) for high-**k** excitons, and suppressed for low-**k** excitons (Fig. 3b). As such, any valley polarization from interlayer tunneling at higher energies (closer to the laser at 1.946 eV) is quickly erased, and the tunneling serves only to uniformly quench both the σ<sup>+</sup> and σ<sup>-</sup> PL spectra. We expect the tunneling to be very efficient at these higher energies owing to resonant interlayer band alignment and regions of hybridization evident in Fig. 1e between the MoSe<sub>2</sub> CB and CrBr<sub>3</sub> *t*<sub>2g</sub> states. This efficient hot electron tunneling will indeed be highly spin polarized, but the comparably fast valley depolarization in MoSe<sub>2</sub> ensures that no signatures persist in the observed DOCP.

We therefore believe that the measured DOCP is sensitive only to spin/valley dynamics in the energy range corresponding to vanishing exciton center-of-mass momentum, close to or inside the light cone. At these low wavevectors, the exchange induced valley depolarization is weak, allowing spin-dependent tunneling to influence the DOCP in luminescence. The fact that DOCP is observed only in the trion state implies that the additional non-radiative decay arising from charge transfer in this low energy range must be slower than the exciton radiative lifetime (sub-ps<sup>54</sup>), but faster than the lifetime of the trion state, which is an order of magnitude longer (>10 ps)<sup>55</sup>. Our conclusion is supported by analysis of the PL linewidths, revealing a magnetization dependent change in the trion linewidth of ~1 meV, while the exciton linewidth remains constant (Fig. 3c). This allows us to estimate that the additional non-radiative decay experienced by the trion owing to spin-dependent charge transfer at these lower energies is ~0.7 ps. The tunneling efficiency is generally influenced by various factors, including band

hybridization, and energy or momentum offsets<sup>9,56–59</sup>. Our calculations (Fig. 1e) predict that at the bottom of the MoSe<sub>2</sub> CB there is a low degree of hybridization with CrBr<sub>3</sub> CB states, and the energy and momentum offsets for possible electron scattering are large. These factors can explain the relatively long charge transfer times deduced from the experiment. We note that the tunneling rates may vary over a large range, as was revealed in recent pump-probe experiments on twisted TMD heterobilayers, where sub-ps to 5 ps tunneling times were observed, drastically dependent on the relative crystallographic twist angle between the layers<sup>57</sup>.

In stark contrast to MoSe<sub>2</sub>, the valley pseudospin lifetime in WSe<sub>2</sub> exceeds the PL lifetime<sup>60</sup>, and so the final PL DOCP will be influenced by the full extent of spin-dependent interlayer tunneling occurring between the laser energy and the PL energy. This explains why the reported DOCP in WSe<sub>2</sub>/CrI<sub>3</sub> structures is larger than our MoSe<sub>2</sub> case, while also explaining why we observe no dependence on laser polarization in our sample (Supplementary Note 5), whereas results from WSe<sub>2</sub>/CrI<sub>3</sub> structures depend fundamentally on the laser polarization<sup>30</sup>.

**Domain-like valley polarization topography.** The intertwined relationship between trion PL and the local magnetization of CrBr<sub>3</sub>, as demonstrated in Fig. 2e, means that the DOCP serves as a proxy magnetization or M-H curve. Viewed in this way, the trion polarization degree bears all the hallmarks of the magnetization response of a thin ferromagnetic film with perpendicular magnetocrystalline anisotropy, in which the magnetization of each domain must be aligned upwards or downwards out of the plane<sup>7,25,61</sup>. When |B| > B<sub>sat</sub> = 50 mT, plateaus are observed, corresponding to magnetic saturation parallel to the external field, whereby the CrBr<sub>3</sub> is essentially in a single magnetic domain state. At field strengths lower than the saturation field, a complex response is observed featuring two marked hysteretic lobes, with a smooth linear gradient around B = 0. Such a dependence is purely the result of magnetic domain dynamics, whereby the two discontinuities at

$B = \pm 20$  mT appear as a result of spontaneous magnetic nucleation<sup>25,61</sup>. This process occurs when a saturating  $B$ -field is gradually removed, until a balance is tipped in favor of the formation of antiparallel adjacent domains, representing a lower energy configuration. For the metastable saturation state to break down, a potential barrier associated with domain wall formation must be overcome<sup>61</sup>.

At very low fields,  $|B| < 20$  mT, the average magnetization responds linearly to  $B$  owing to unopposed lateral domain wall motion through the flake, allowing domains to grow and shrink as appropriate. As the  $\text{CrBr}_3$  flake is a single crystal, domain wall motion ought to be generally unobstructed, in contrast to polycrystalline thin-film ferromagnets, in which grain boundaries may impede domain growth<sup>62</sup>. Introducing certain defects and disorder to the flake may also lead to domain wall pinning which opens up a hysteresis loop at zero field, consistent with the more typical remanence signatures of conventional ferromagnets<sup>4,30</sup>. As such, the absence of coercivity in this sample indicates both a weak anisotropy<sup>24</sup>, and a low density of defects of the type which may impede lateral domain wall motion<sup>61,63</sup>. However, we note that there may be a high density of other defects which have a weaker influence on domain dynamics, consistent with the unstable nature of  $\text{CrBr}_3$  (see Supplementary Note 8).

The crucial consequence of these  $\text{CrBr}_3$  domain dynamics is that the spin-dependent interlayer charge transfer in the heterostructure adopts a spatial topography and magnetic response describable by the physics of ferromagnetic domains. As shown in Fig. 4a, when  $B > B_{\text{sat}}$  ( $B < -B_{\text{sat}}$ ), the charge transfer is preferentially spin- $\downarrow$  (spin- $\uparrow$ ) over the entire interface. However, when  $|B| < B_{\text{sat}}$ , the interlayer charge transfer rates adopt a highly contrasting spatial arrangement over the sample, which in turn creates domain-like regions of opposite valley polarization co-existing in the  $\text{MoSe}_2$  trion population. Cumulatively, a reversal of the external  $B$ -field gives efficient selectivity between opposite preferential tunneling rates for electrons of spin- $\uparrow$  or spin- $\downarrow$ , while control of the field strength close to zero allows fine-tuning of their relative prevalence.

We note that in our PL experiments, we measure an average of domain activity within the area of our laser spot,  $\sim 5 \mu\text{m}^2$ . In order to gain insight into the characteristic length scales of the trion valley polarization domains in our sample, we measure the local magnetization via the polar magneto-optical Kerr effect (MOKE) in an optical microscope utilizing broadband illumination and wide-field high spatial resolution detection (Fig. 4b). We expect that the polar Kerr signal arises mainly from the  $\text{CrBr}_3$  layers of

the sample, given the maximum of the illumination energy at 2.7 eV closely matches the  $\text{CrBr}_3$  main absorption resonance at 2.5 eV<sup>37</sup>. Therefore, the close agreement between the PL from  $\text{MoSe}_2$  and the Kerr signal indicates a robust proximity effect and strong layer interaction<sup>64</sup>. Despite our MOKE measurement area being  $\sim 0.5 \mu\text{m}^2$ , an order of magnitude smaller than in the PL experiment, there is close agreement between the two magneto-optical techniques, indicating that the domains are significantly smaller than the length scales of our optical probes. Indeed, no domain activity could be resolved in the Kerr microscope at all, confirming a domain size smaller than the optical resolution of the system,  $\sim 400$  nm (See Supplementary Note 8). High spatial resolution techniques such as scanning probe magnetometry would be required to resolve the domain structure in our sample<sup>5,65</sup>.

Our findings are in good agreement with previous work on  $\text{CrBr}_3$  flakes in which electron microscopy reveals stripe domains with widths between 20 and 200 nm<sup>66</sup>. In thin-film ferromagnets such as our  $\text{CrBr}_3$  flake, the domain size is governed by a complex interplay between magnetocrystalline and shape anisotropies, domain wall width, in-plane remanence, exchange energy, and magnetostatic interaction energy between the top and bottom film surfaces<sup>67</sup>. The domain dynamics will therefore depend sensitively on the specific balance of these parameters, leading to significant variation. Indeed, complex and diverse domain patterns have been observed in  $\text{CrBr}_3$  including stripe, honeycomb, bubble, and cone domain structures<sup>68</sup>. Weak in-plane external  $B$ -field orientation, disorder, temperature, or unpredictable local fluctuations, can all influence the domain patterns formed during each  $B$ -field cycle, with no correlation expected between patterns present before and after each instance of saturation, unless external input is used to provide control<sup>68</sup>. We note that the trion Bohr radius in  $\text{MoSe}_2$  ( $\sim 1$  nm), is 1–2 orders of magnitude smaller than the domain sizes inferred by our observations. This suggests that control of domain formation dynamics in  $\text{CrBr}_3$ , by the techniques mentioned above, would generate desired spatial patterns of contrasting electronic and trionic spin-valley polarization in  $\text{MoSe}_2$ , be they stripe, honeycomb, bubble, and so on, with important consequences for opto-spintronic device design at the nanoscale.

## Discussion

To conclude, we observe spectrally dependent magnetic proximity effects in photoluminescence from monolayer  $\text{MoSe}_2$  in contact with few-layer  $\text{CrBr}_3$ . The local out of plane

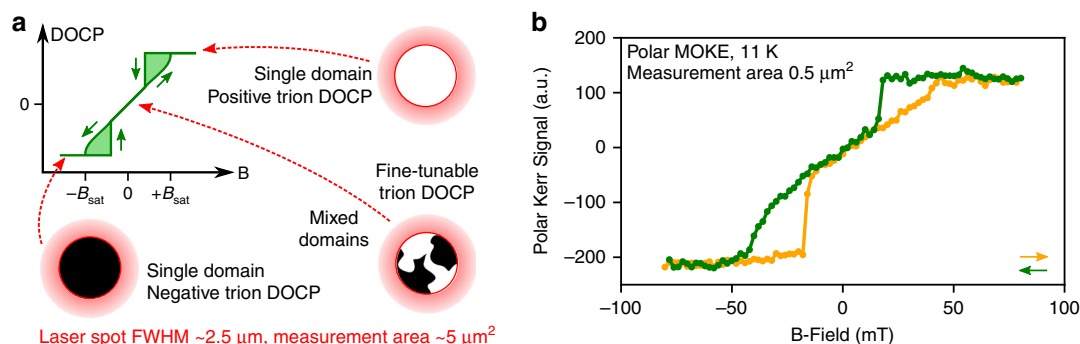


**Fig. 4** Domain-like arrangement of trion valley polarization. **a** Illustration of the trion degree of circular polarization (DOCP), with indications of the spatial arrangement of trion valley polarization at various points on the curve. Above  $|B_{\text{sat}}|$ , the  $\text{CrBr}_3$  is in a single domain state and there is a uniform spin preference for electron tunneling from  $\text{MoSe}_2$  to  $\text{CrBr}_3$ . At lower  $B$ -fields, the relative strengths of spin  $\uparrow$  or  $\downarrow$  tunneling may be fine-tuned by control of the external field, which determines the relative spatial area occupied by adjacent domains. The red circles indicate an approximation of the laser spot area in the PL study, about  $5 \mu\text{m}^2$ , over which the domain behavior is averaged. **b** Polar magneto-optical Kerr effect (MOKE) signal from the same sample, with a much smaller measurement area of  $0.5 \mu\text{m}^2$ . The domain nucleation behavior is retained, indicating a very small length scale of domains.

magnetization in CrBr<sub>3</sub> is imprinted in the MoSe<sub>2</sub> trion state valley polarization, while the neutral exciton state bears no hallmarks of proximity interactions. We attribute the observed magneto-optical response to a spin-dependent interlayer charge transfer process, whereby electrons tunnel from the CB of MoSe<sub>2</sub> into the CB of CrBr<sub>3</sub> with differing rates depending on their real spin. This leaves the optically pumped exciton population in MoSe<sub>2</sub> subject to competing mechanisms of spin-dependent tunneling and valley pseudospin depolarization, ultimately leading to the observed charge-state dependency of the proximity effects in photoluminescence. Furthermore, we infer that in the absence of an applied *B*-field, the sample displays simultaneous manifestation of positive and negative valley polarization in the trion population, with an intricate spatial topography conforming to the magnetic domains of CrBr<sub>3</sub>.

Our results demonstrate a highly localized (<400 nm) technique to engineer the interlayer tunneling rates of electrons in van der Waals heterostructures. The wide-ranging implications of this extend to, for example, incorporation of a layered ferromagnet beneath a TMD heterobilayer to enable control of the interlayer exciton lifetime, or local spin and charge densities, serving as a powerful complementary technique to the design of the crystallographic twist angle. Such enticing avenues of band structure engineering are yet to be explored. A further tantalizing possibility is the mimicry of unconventional spin textures by 2-dimensional semiconductors in proximity to magnetic materials. The local sensitivity of excitonic valley polarization may be extended to employ monolayer MoSe<sub>2</sub> as an atomically thin optical probe for such exotic phenomena as skyrmions or domain wall racetrack devices, thus realizing a wealth of far-reaching consequences along the boundary between exciton physics and van der Waals spintronics.

## Methods

**Low-temperature magneto-optical spectroscopy.** Low-temperature photoluminescence spectroscopy was performed by mounting the sample in a liquid helium bath cryostat at 4.2 K with free-space optical access and a superconducting magnet coil. Non-resonant continuous-wave excitation at 1.946 eV in either  $\sigma^+$  or  $\sigma^-$  circular polarization was used, along with helicity selective circularly polarized PL collection, directed through a 0.75 m spectrometer and onto a nitrogen-cooled high sensitivity charge-coupled device. The helicity of the laser has no influence on the results measured, as discussed in Supplementary Note 5. To obtain linewidths and valley Zeeman splitting of exciton and trion peaks, Gaussian peak fitting was carried out on the PL spectra, as discussed in Supplementary Note 6.

**Density functional theory calculations.** See Supplementary Notes 1 and 2.

**Low-temperature wide field Kerr microscopy.** Spatially resolved polar Kerr hysteresis loops were acquired at low temperature using a wide field Kerr microscope equipped with a small helium gas flow cryostat designed for microscopy. A long working distance, high numerical aperture (NA 0.7) objective lens was used to achieve a spatial resolution of 400 nm. Spatial stability was achieved by mounting the cryostat on a piezoelectric stage for active drift correction. Hysteresis loops were acquired from user defined microscale regions of interest on the sample. The polar Kerr effect allowed sensitivity to the out-of-plane component of the magnetization in response to a magnetic field as it was swept perpendicular to the sample plane. The sample illumination was linearly polarized, while polarization changes of the reflected light due to the polar Kerr effect were detected as intensity changes using a high sensitivity CMOS camera after the light was passed through a nearly crossed analyzer. A background polarization rotation that was linear in applied field was measured from the sample substrate and subtracted from the acquired loops. The background was due to the Faraday rotation in the objective lens and cryostat window when subject to a field applied parallel to the polar axis. Differential imaging allowed non-magnetic contrast such as sample topography to be subtracted leaving only the contrast due to the out-of-plane component of the sample magnetization.

**Sample fabrication.** A heterostructure comprising of MoSe<sub>2</sub>/CrBr<sub>3</sub> encapsulated within thin hexagonal boron nitride (hBN) layers was assembled on a DBR substrate (top layer ~100 nm SiO<sub>2</sub>) following standard dry transfer procedures using a poly (methyl methacrylate) (PMMA) membrane. MoSe<sub>2</sub> crystals were exfoliated on

290 nm SiO<sub>2</sub>/Si substrate and monolayers of MoSe<sub>2</sub> were identified using optical contrast and room temperature PL measurements. To begin the heterostructure assembly, first, a monolayer of MoSe<sub>2</sub> was picked up by a thin hBN (~8–10 nm) using the PMMA membrane. CrBr<sub>3</sub> crystals, purchased from commercial supplier HQ Graphene, were exfoliated on to a 290 nm SiO<sub>2</sub>/Si substrate in an argon-filled glove box maintaining the water and oxygen concentration less than 0.1 ppm. CrBr<sub>3</sub> flakes of different thicknesses (2–6 layers) could be easily identified using the contrast variation under different color filters and dark-field imaging. However, for this work, a relatively thick ~7–8 nm thick flake was used. A suitable (uniform and crack free) CrBr<sub>3</sub> layer was picked up by MoSe<sub>2</sub>/hBN/PMMA membrane in the glove box prepared in the first step. To complete the encapsulation of MoSe<sub>2</sub>/CrBr<sub>3</sub> between hBN layers, a thin hBN layer was further picked up by this membrane. Finally, the complete stack (hBN/CrBr<sub>3</sub>/MoSe<sub>2</sub>/hBN) on PMMA was dropped onto a DBR mirror by cutting the PMMA membrane. The PMMA was washed away in acetone and in IPA.

## Data availability

Experimental data from this work is stored on University of Sheffield central file servers and is available on request by contacting the corresponding authors.

Received: 23 March 2020; Accepted: 30 October 2020;

Published online: 26 November 2020

## References

- Zhou, J. et al. A library of atomically thin metal chalcogenides. *Nature* **556**, 355–359 (2018).
- Haastrup, S. et al. The computational 2D materials database: high-throughput modeling and discovery of atomically thin crystals. *2D Mater.* **5**, 042002 (2018).
- Gong, C. et al. Discovery of intrinsic ferromagnetism in two-dimensional van der Waals crystals. *Nature* **546**, 265–269 (2017).
- Huang, B. et al. Layer-dependent ferromagnetism in a van der Waals crystal down to the monolayer limit. *Nature* **546**, 270–273 (2017).
- Fei, Z. et al. Two-dimensional itinerant ferromagnetism in atomically thin Fe<sub>3</sub>GeTe<sub>2</sub>. *Nat. Mater.* **17**, 778–782 (2018).
- Lee, J.-U. et al. Ising-type magnetic ordering in atomically thin FePS<sub>3</sub>. *Nano Lett.* **16**, 7433–7438 (2016).
- Kim, M. et al. Micromagnetometry of two-dimensional ferromagnets. *Nat. Electron.* **2**, 457–463 (2019).
- Geim, A. K. & Grigorieva, I. V. Van der Waals heterostructures. *Nature* **499**, 419–425 (2013).
- Alexeev, E. M. et al. Resonantly hybridized excitons in moiré superlattices in van der Waals heterostructures. *Nature* **567**, 81–86 (2019).
- Jin, C. et al. Imaging of pure spin-valley diffusion current in WS<sub>2</sub>-WSe<sub>2</sub> heterostructures. *Science* **360**, 893–896 (2018).
- Cao, Y. et al. Unconventional superconductivity in magic-angle graphene superlattices. *Nature* **556**, 43–50 (2018).
- Yu, H., Liu, G.-B., Tang, J., Xu, X. & Yao, W. Moiré excitons: from programmable quantum emitter arrays to spin-orbit-coupled artificial lattices. *Sci. Adv.* **3**, e1701696 (2017).
- Hunt, B. et al. Massive Dirac fermions and Hofstadter butterfly in a van der Waals heterostructure. *Science* **340**, 1427–1430 (2013).
- Sharpe, A. L. et al. Emergent ferromagnetism near three-quarters filling in twisted bilayer graphene. *Science* **365**, 605–608 (2019).
- Huang, B. et al. Electrical control of 2D magnetism in bilayer CrI<sub>3</sub>. *Nat. Nanotechnol.* **13**, 544–548 (2018).
- Gong, C. & Zhang, X. Two-dimensional magnetic crystals and emergent heterostructure devices. *Science* **363**, eaav4450 (2019).
- Burch, K. S., Mandrus, D. & Park, J.-G. Magnetism in two-dimensional van der Waals materials. *Nature* **563**, 47–52 (2018).
- Seyler, K. L. et al. Ligand-field helical luminescence in a 2D ferromagnetic insulator. *Nat. Phys.* **14**, 277–281 (2018).
- Gibertini, M., Koperski, M., Morpurgo, A. & Novoselov, K. Magnetic 2D materials and heterostructures. *Nat. Nanotechnol.* **14**, 408–419 (2019).
- Jiang, S., Li, L., Wang, Z., Mak, K. F. & Shan, J. Controlling magnetism in 2D CrI<sub>3</sub> by electrostatic doping. *Nat. Nanotechnol.* **13**, 549–553 (2018).
- Mak, K. F., Shan, J. & Ralph, D. C. Probing and controlling magnetic states in 2D layered magnetic materials. *Nat. Rev. Phys.* **1**, 646–661 (2019).
- Zhong, D. et al. Layer-resolved magnetic proximity effect in van der Waals heterostructures. *Nat. Nanotechnol.* **15**, 187–191 (2020).
- Ghazaryan, D. et al. Magnon-assisted tunnelling in van der Waals heterostructures based on CrBr<sub>3</sub>. *Nat. Electron.* **1**, 344–349 (2018).
- Ciorciaro, L., Kroner, M., Watanabe, K., Taniguchi, T. & Imamoglu, A. Observation of magnetic proximity effect using resonant optical spectroscopy



- of an electrically tunable MoSe<sub>2</sub>/CrBr<sub>3</sub> heterostructure. *Phys. Rev. Lett.* **124**, 197401 (2020).
25. Zhang, Z. et al. Direct photoluminescence probing of ferromagnetism in monolayer two-dimensional CrBr<sub>3</sub>. *Nano Lett.* **19**, 3138–3142 (2019).
  26. Chen, W. et al. Direct observation of van der Waals stacking-dependent interlayer magnetism. *Science* **366**, 983–987 (2019).
  27. Tsubokawa, I. On the magnetic properties of a CrBr<sub>3</sub> single crystal. *J. Phys. Soc. Jpn.* **15**, 1664–1668 (1960).
  28. Klein, D. R. et al. Enhancement of interlayer exchange in an ultrathin two-dimensional magnet. *Nat. Phys.* **15**, 1255–1260 (2019).
  29. Xu, X., Yao, W., Xiao, D. & Heinz, T. F. Spin and pseudospins in layered transition metal dichalcogenides. *Nat. Phys.* **10**, 343–350 (2014).
  30. Zhong, D. et al. Van der Waals engineering of ferromagnetic semiconductor heterostructures for spin and valleytronics. *Sci. Adv.* **3**, e1603113 (2017).
  31. Tong, Q., Chen, M. & Yao, W. Magnetic proximity effect in a van der Waals moiré superlattice. *Phys. Rev. Appl.* **12**, 024031 (2019).
  32. Seyler, K. L. et al. Valley manipulation by optically tuning the magnetic proximity effect in WSe<sub>2</sub>/CrI<sub>3</sub> heterostructures. *Nano Lett.* **18**, 3823–3828 (2018).
  33. Momma, K. & Izumi, F. VESTA 3 for three-dimensional visualization of crystal, volumetric and morphology data. *J. Appl. Crystallogr.* **44**, 1272–1276 (2011).
  34. Shcherbakov, D. et al. Raman spectroscopy, photocatalytic degradation, and stabilization of atomically thin chromium tri-iodide. *Nano Lett.* **18**, 4214–4219 (2018).
  35. Ross, J. S. et al. Electrical control of neutral and charged excitons in a monolayer semiconductor. *Nat. Commun.* **4**, 1474 (2013).
  36. Drüppel, M., Deilmann, T., Krüger, P. & Rohlfing, M. Diversity of trion states and substrate effects in the optical properties of an MoS<sub>2</sub> monolayer. *Nat. Commun.* **8**, 2117 (2017).
  37. Molina-Sánchez, A., Catarina, G., Sangalli, D. & Fernandez-Rossier, J. Magneto-optical response of chromium trihalide monolayers: chemical trends. *J. Mater. Chem. C* **8**, 8856–8863 (2020).
  38. Bermudez, V. M. & McClure, D. S. Spectroscopic studies of the two-dimensional magnetic insulators chromium trichloride and chromium tribromide-I. *J. Phys. Chem. Solids* **40**, 129–147 (1979).
  39. Dillon Jr, J., Kamimura, H. & Remeika, J. Magneto-optical properties of ferromagnetic chromium trihalides. *J. Phys. Chem. Solids* **27**, 1531–1549 (1966).
  40. Dillon Jr, J., Kamimura, H. & Remeika, J. Magneto-optical studies of chromium tribromide. *J. Appl. Phys.* **34**, 1240–1245 (1963).
  41. Lado, J. L. & Fernández-Rossier, J. On the origin of magnetic anisotropy in two dimensional CrI<sub>3</sub>. *2D Mater.* **4**, 035002 (2017).
  42. Gudelli, V. K. & Guo, G.-Y. Magnetism and magneto-optical effects in bulk and few-layer CrI<sub>3</sub>: a theoretical GGA+U study. *N. J. Phys.* **21**, 053012 (2019).
  43. Zollner, K., Faria Junior, P. E. & Fabian, J. Proximity exchange effects in MoSe<sub>2</sub> and WSe<sub>2</sub> heterostructures with CrI<sub>3</sub>: Twist angle, layer, and gate dependence. *Phys. Rev. B* **100**, 085128 (2019).
  44. Li, Y. et al. Valley splitting and polarization by the Zeeman effect in monolayer MoSe<sub>2</sub>. *Phys. Rev. Lett.* **113**, 266804 (2014).
  45. Wang, G. et al. Magneto-optics in transition metal diselenide monolayers. *2D Mater.* **2**, 034002 (2015).
  46. Yu, H., Cui, X., Xu, X. & Yao, W. Valley excitons in two-dimensional semiconductors. *Nat. Sci. Rev.* **2**, 57–70 (2015).
  47. Kormányos, A. et al. k-p theory for two-dimensional transition metal dichalcogenide semiconductors. *2D Mater.* **2**, 022001 (2015).
  48. Lyons, T. P. et al. The valley Zeeman effect in inter- and intra-valley trions in monolayer WSe<sub>2</sub>. *Nat. Commun.* **10**, 2330 (2019).
  49. Korenev, V. et al. Dynamic spin polarization by orientation-dependent separation in a ferromagnet–semiconductor hybrid. *Nat. Commun.* **3**, 959 (2012).
  50. Glazov, M. et al. Exciton fine structure and spin decoherence in monolayers of transition metal dichalcogenides. *Phys. Rev. B* **89**, 201302 (2014).
  51. Yu, H., Liu, G.-B., Gong, P., Xu, X. & Yao, W. Dirac cones and Dirac saddle points of bright excitons in monolayer transition metal dichalcogenides. *Nat. Commun.* **5**, 3876 (2014).
  52. Maialle, M., e Silva, Ed. A. & Sham, L. Exciton spin dynamics in quantum wells. *Phys. Rev. B* **47**, 15776 (1993).
  53. Dufferwiel, S. et al. Valley-addressable polaritons in atomically thin semiconductors. *Nat. Photonics* **11**, 497–501 (2017).
  54. Jakubczyk, T. et al. Radiatively limited dephasing and exciton dynamics in MoSe<sub>2</sub> monolayers revealed with four-wave mixing microscopy. *Nano Lett.* **16**, 5333–5339 (2016).
  55. Godde, T. et al. Exciton and trion dynamics in atomically thin MoSe<sub>2</sub> and WSe<sub>2</sub>: Effect of localization. *Phys. Rev. B* **94**, 165301 (2016).
  56. Ovesen, S. et al. Interlayer exciton dynamics in van der Waals heterostructures. *Commun. Phys.* **2**, 23 (2019).
  57. Merkl, P. et al. Ultrafast transition between exciton phases in van der Waals heterostructures. *Nat. Mater.* **18**, 691–696 (2019).
  58. Froehlicher, G., Lorchat, E. & Berciaud, S. Charge versus energy transfer in atomically thin graphene-transition metal dichalcogenide van der Waals heterostructures. *Phys. Rev. X* **8**, 011007 (2018).
  59. Selig, M., Malic, E., Ahn, K. J., Koch, N. & Knorr, A. Theory of optically induced Förster coupling in van der Waals coupled heterostructures. *Phys. Rev. B* **99**, 035420 (2019).
  60. Zhu, C. et al. Exciton valley dynamics probed by Kerr rotation in WSe<sub>2</sub> monolayers. *Phys. Rev. B* **90**, 161302 (2014).
  61. Jagla, E. A. Hysteresis loops of magnetic thin films with perpendicular anisotropy. *Phys. Rev. B* **72**, 094406 (2005).
  62. Riedi, P. & Zanghi-Mangion, I. Difference between domain wall motion in single crystal and polycrystalline YIG observed by pulsed NMR. *Phys. Status Solidi A, Appl. Res.* **87**, K163–K166 (1985).
  63. Jeudy, V., Pardo, R. D., Torres, W. S., Bustingorry, S. & Kolton, A. Pinning of domain walls in thin ferromagnetic films. *Phys. Rev. B* **98**, 054406 (2018).
  64. Catarina, G., Peres, N. & Fernández-Rossier, J. Magneto-optical Kerr effect in spin split two-dimensional massive Dirac materials. *2D Mater.* **7**, 025011 (2020).
  65. Thiel, L. et al. Probing magnetism in 2D materials at the nanoscale with single-spin microscopy. *Science* **364**, 973–976 (2019).
  66. Matricardi, V., Lehmann, W., Kitamura, N. & Silcox, J. Electron microscope observations of ferromagnetic domains in chromium tribromide. *J. Appl. Phys.* **38**, 1297–1298 (1967).
  67. Virost, F., Favre, L., Hayn, R. & Kuz'Min, M. Theory of magnetic domains in uniaxial thin films. *J. Phys. D: Appl. Phys.* **45**, 405003 (2012).
  68. Kuhlow, B. & Lambeck, M. Magnetic domain structures in CrBr<sub>3</sub>. *Physica B +C* **80**, 365–373 (1975).

## Acknowledgements

T. P. L. acknowledges financial support from the EPSRC Doctoral Prize Fellowship scheme under Grant Reference EP/R513313/1. T. P. L., K. S. N. and A. I. T. acknowledge financial support from the European Graphene Flagship Projects under grant agreements 785219 and 881603, and EPSRC grants EP/P026850/1 and EP/S030751/1. K. S. N. also acknowledges support from EU Quantum Technology Flagship Programs, European Research Council Synergy Grant Hetero2D, the Royal Society, EPSRC grants EP/N010345/1, EP/S030719/1. We gratefully acknowledge the Exeter Time-Resolved Magnetism Facility (EXTREMAG - EPSRC Grant Reference EP/R008809/1) for the time allocated to this study for low temperature, wide-field Kerr microscopy. The DFT calculations were performed on the Tirant III cluster of the Servei d'Informàtica of the University of Valencia (project vlc82) and on Mare Nostrum cluster of the Barcelona Supercomputing Center (project FI-2019-2-0034). A.M.-S. acknowledges the Marie-CurieCOFUND program Nano TRAIN For Growth II (Grant Agreement 713640). J.F.-R. acknowledges financial support from FCT for the grant UTAP-EXPL/NTec/0046/2017, as well as Generalitat Valenciana funding Prometeo 2017/139 and MINECO-Spain (Grant no. MAT2016-78625-C2). Growth of hexagonal boron nitride crystals was supported by the Elemental Strategy Initiative conducted by the MEXT, Japan, and the CREST (JPMJCR15F3), J.S.T.

## Author contributions

T.P.L. and D.G. carried out photoluminescence experiments. T.P.L., P.S.K., and F.W. carried out Kerr effect experiments. A.M.-S. and J.F.-R. carried out density functional theory calculations. T.P.L., D.G., and A.I.T. analyzed the experimental data. A.M., F.W., and A.K. fabricated the samples. T.T. and K.W. synthesized high-quality hexagonal boron nitride for all samples. K.S.N., J.F.-R., and A.I.T. managed various aspects of the project. T.P.L. wrote the manuscript. A.I.T. supervised the project.

## Competing interests

The authors declare no competing interests.

## Additional information

Supplementary information is available for this paper at <https://doi.org/10.1038/s41467-020-19816-4>.

Correspondence and requests for materials should be addressed to T.P.L. or A.I.T.

Peer review information *Nature Communications* thanks the anonymous reviewer(s) for their contribution to the peer review of this work.

Reprints and permission information is available at <http://www.nature.com/reprints>

Publisher's note Springer Nature remains neutral with regard to jurisdictional claims in published maps and institutional affiliations.





**Open Access** This article is licensed under a Creative Commons Attribution 4.0 International License, which permits use, sharing, adaptation, distribution and reproduction in any medium or format, as long as you give appropriate credit to the original author(s) and the source, provide a link to the Creative Commons license, and indicate if changes were made. The images or other third party material in this article are included in the article's Creative Commons license, unless indicated otherwise in a credit line to the material. If material is not included in the article's Creative Commons license and your intended use is not permitted by statutory regulation or exceeds the permitted use, you will need to obtain permission directly from the copyright holder. To view a copy of this license, visit <http://creativecommons.org/licenses/by/4.0/>.

© The Author(s) 2020